Hindawi
International Journal of Antennas and Propagation
Volume 2022, Article ID 2594853, 11 pages
https://doi.org/10.1155/2022/2594853

Research Article

A Microwave Imaging Matrix Algorithm Based on Contrast Source

Meng Wang, Guizhen Lu, and Junwen Chen

School of Information and Communication Engineering, Communication University of China, Beijing 100024, China

Correspondence should be addressed to Meng Wang; wangmeng1993@cuc.edu.cn

Received 5 March 2022; Revised 1 May 2022; Accepted 18 May 2022; Published 8 June 2022

Academic Editor: Luca Catarinucci

A microwave imaging matrix algorithm based on the contrast source is proposed. It is known that the contrast source and the total field change by shifting the position of the incident field. To ensure the constancy of the contrast source, this paper first proposes a novel inversion model based on the contrast source. The excitation source is located at a single fixed position, and the scattering data is obtained by measuring points evenly distributed on multiple circular layers. Secondly, a matrix algorithm based on the contrast source is proposed, which transforms the nonlinear imaging problem into a matrix operation step-by-step without iteration. The numerical simulation results show that the matrix algorithm proposed in this paper has high precision and good performance with complex imaging problems. In addition, the limitation of the proposed algorithm when inversing data with noise is also analyzed.

1. Introduction

Microwave imaging is one of the classic inverse problems, which has been extensively utilized in earth exploration, medical diagnosis, metasurface antenna, and more [1, 2]. The core of the microwave imaging problem is to resolve the parameters of the scatterer, such as its material coefficient, position, and shape, through data obtained from the scattering field. At present, many common imaging algorithms are based on the Lippmann–Schwinger equation. Owing to its nonlinearity and highly ill-condition characteristics, this equation introduces certain difficulties to the solution process.

Commonly used microwave imaging algorithms mainly include stochastic optimization algorithms [3], such as particle swarm optimization (PSO), genetic algorithms (GA), and differential evolution (DE); algorithms based on gradient theory, such as contrast source inversion (CSI) [4, 5] and the subspace optimization method (SOM) [6, 7]; and imaging algorithms based on other methods, such as compressive sensing (CS) [8] and deep learning [9]. In addition, some other nonlinear estimation methods have also achieved good performance in inverse scattering problems. [10].

Many imaging algorithms involve iteration. Although traditional iterative methods can effectively solve the microwave imaging problem, the time and hardware costs are high. In addition, the microwave imaging problem is a strict physical field problem, and however, many imaging algorithms focus solely on the modification of algorithm parameters and the addition of regular terms, ignoring the connection with the physical process [9]. The CSI method is a classic imaging algorithm. It is known that the contrast source is closely related to the total field [4].

In this paper, a microwave imaging matrix algorithm based on the contrast source is proposed. The contrast source and the total field will be affected by differences in the incident field position. As such, an improved inversion model is first proposed, where the position of the excitation source is kept fixed, and measurement points are evenly distributed on circles of different radius, which ensures the consistency of the contrast source. Then, the matrix algorithm is proposed which converts the nonlinear imaging problem into a matrix problem of several steps without iteration, effectively reducing the solution cost and increasing its suitability for complex imaging problems. And the matrix algorithm proposed has a high accuracy and strict physical significance. In addition, the matrix algorithm has a higher solution efficiency than the hybrid algorithm proposed in [11].

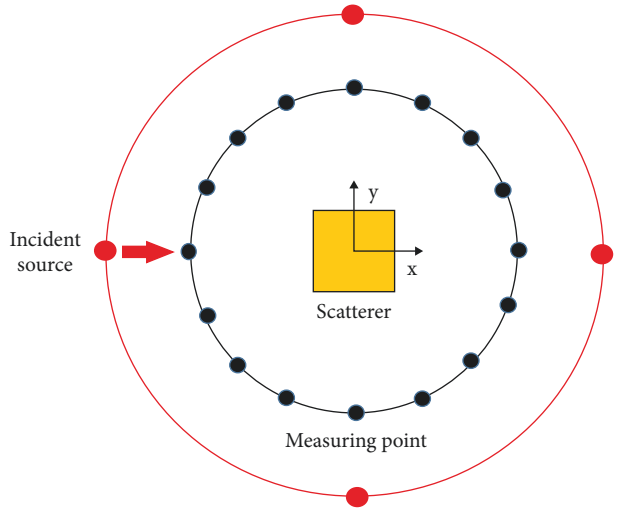

Figure 1: Traditional measurement model of microwave imaging.

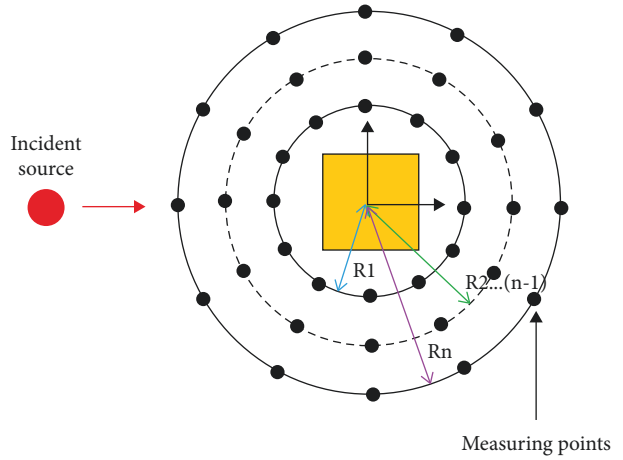

Figure 2: Improved inversion model.

The sections of this paper are arranged as follows. Section 2 introduces an improved inversion model. Section 3 introduces the microwave imaging matrix algorithm. In Section 4, different types of scatterers are utilized to assess the performance of the proposed matrix algorithm. Finally, the present work is summarized, and the direction of further research is indicated.

2. Improved Inversion Model

The traditional microwave imaging measurement model is shown in Figure 1.

In the traditional model, the scatterer is located in the imaging domain, and the background is the free space. Several measurement points for the detection of scattered field signals are evenly distributed on a single circle. This model uses several excitation sources arranged on a circle with a fixed radius for multi-position incidence.

The physical meaning of the contrast source is the result of multiplying the total field in the imaging domain with material parameters, just as in the following equation [4]. For nonmagnetic materials, the material parameter is usually the value of the relative permittivity.

$$Cs = \chi \cdot u^{\text{tot}}, \tag{1}$$

where Cs represents the contrast source, χ is the contrast function, and u^{tot} is the total field.

In reference [12], a modified inversion model was proposed to improve the accuracy of inversion. In the modified model, several measurement points distributed on the circumference of multilayers were applied. However, this measurement model did not establish a relationship with the physical quantity "contrast source". Meanwhile, this model did not consider the constancy of the contrast source.

Under the Born approximation, the total field u^{tot} can be approximated by the incident field u^{inc}, so the contrast source has an obvious numerical relationship with the data of the incident field. Therefore, an improved inversion model is proposed which is shown in the following Figure 2.

where $R1$, $R2\ldots(n-1)$, and Rn represent different radius of the measurement circumferences, respectively.

In order to facilitate calculation and simulation verification conveniently, the number of receiving circles in this paper is set to 3, that is, n is equal to 3.

In the improved model, there is only one excitation source, and its position is fixed. The data of the scattered field can be obtained from measuring points uniformly distributed on concentric circular arrangements. With the incident source in a single fixed position, material parameters and the incident field are constant. Therefore, the contrast source is the same whether it is employed to image the scatterer or calculate the total field inside the scatterer. This condition of the consistent contrast source allows for the effective simplification of the calculation process. In addition, the consistency of contrast source, which can be applied to solve the inversion of the relative permittivity, is the basis of the matrix algorithm.

3. Microwave Imaging Matrix Algorithm

The vector electromagnetic field problem in two-dimensional space can be transformed into a problem of calculating the components of the electromagnetic field, which can in turn be further simplified to scalar integral equation, effectively reducing the amount of calculation required. Using the notation of reference [4], the electric field integral equation is as follows:

$$u^{\text{tot}}(\vec{p}) = u^{\text{inc}}(\vec{p}) + k^2 \int_D G(\vec{p}, \vec{q}) \chi(\vec{q}) u^{\text{tot}}(\vec{q}) \mathrm{d}v, \tag{2}$$

where $\vec{p}$ and $\vec{q}$ represent position vectors in two-dimensional space, $u^{\text{tot}}(\vec{p})$ represents the total field, $u^{\text{inc}}(\vec{p})$ represents the incident field, D is the imaging domain, $\chi(\vec{q})$ is the contrast function, and other physical quantities satisfy the following relationships.

$$\begin{aligned} k &= \omega \sqrt{\varepsilon_0 \mu_0}, \\ G(\vec{p}, \vec{q}) &= \frac{i}{4} H_0^{(1)}(k|\vec{p} - \vec{q}|), \end{aligned} \tag{3}$$

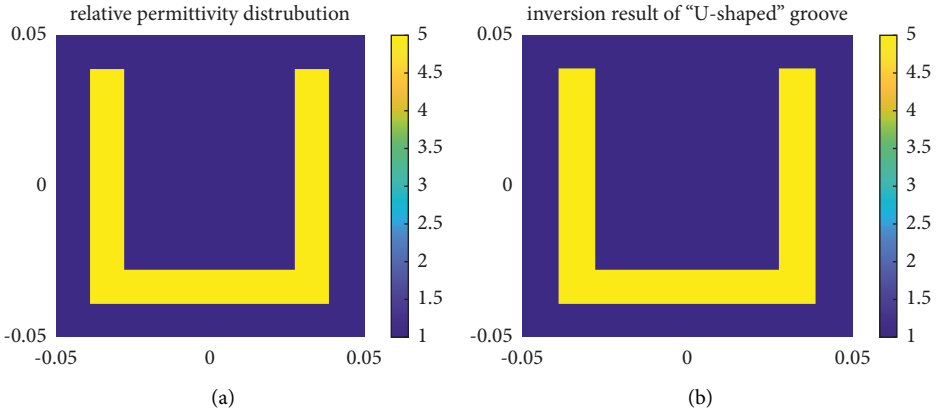

FIGURE 3: Comparison results of the relative permittivity distribution of the *"U-shaped"* groove.

where k is the wave vector, ω is the angular frequency, μ is the magnetic permeability, ε is the permittivity, and $H_0^{(1)}$ represents the first-order Hankel function.

Equation (1) can be written in vector form as to conform to the symbol from reference [4] as follows:

$$Cs(\vec{q}) = \chi(\vec{q})u^{\text{tot}}(\vec{q}), \tag{4}$$

with the vector $\vec{q}$ defined as $(\vec{r}^{\,d}_1 \cdots \vec{r}^{\,d}_m)^T$, where the $\vec{r}^{\,d}$ are position coordinates inside the scatterer.

The above formula can be written in the matrix form.

$$\begin{bmatrix} Cs\left(\vec{r}^{\,d}_1\right) \\ \vdots \\ Cs\left(\vec{r}^{\,d}_m\right) \end{bmatrix} = \begin{bmatrix} \chi_1 & 0 & 0 \\ 0 & \ddots & 0 \\ 0 & 0 & \chi_m \end{bmatrix} \begin{bmatrix} u^{\text{tot}}\left(\vec{r}^{\,d}_1\right) \\ \vdots \\ u^{\text{tot}}\left(\vec{r}^{\,d}_m\right) \end{bmatrix}. \tag{5}$$

Therefore, the scattered field signal can be expressed using the contrast source, as follows:

$$u^{\text{sca}}(\vec{p}) = k^2 \int_D G(\vec{p}, \vec{q}) \cdot Cs(\vec{q}) \mathrm{d}v, \tag{6}$$

where $u^{\text{sca}}(\vec{p}) = u^{\text{tot}}(\vec{p}) - u^{\text{inc}}$, with the vector $\vec{p}$ defined as $(\vec{r}^{\,s}_1 \cdots \vec{r}^{\,s}_n)^T$ where the $\vec{r}^{\,s}$ are position coordinates of the scattering area.

The matrix form of the above formula is as follows:

$$\begin{bmatrix} u^{\text{sca}}\left(\vec{r}^{\,s}_1\right) \\ u^{\text{sca}}\left(\vec{r}^{\,s}_2\right) \\ \vdots \\ u^{\text{sca}}\left(\vec{r}^{\,s}_{n-1}\right) \\ u^{\text{sca}}\left(\vec{r}^{\,s}_n\right) \end{bmatrix} = \begin{bmatrix} \mathbf{Z}\left(\vec{r}^{\,s}_1, \vec{r}^{\,d}_1\right) & \cdots & \mathbf{Z}\left(\vec{r}^{\,s}_1, \vec{r}^{\,d}_m\right) \\ \mathbf{Z}\left(\vec{r}^{\,s}_2, \vec{r}^{\,d}_1\right) & & \mathbf{Z}\left(\vec{r}^{\,s}_2, \vec{r}^{\,d}_m\right) \\ \vdots & \ddots & \\ \mathbf{Z}\left(\vec{r}^{\,s}_{n-1}, \vec{r}^{\,d}_1\right) & & \\ \mathbf{Z}\left(\vec{r}^{\,s}_n, \vec{r}^{\,d}_1\right) & \cdots & \mathbf{Z}\left(\vec{r}^{\,s}_n, \vec{r}^{\,d}_m\right) \end{bmatrix} \begin{bmatrix} Cs\left(\vec{r}^{\,d}_1\right) \\ \vdots \\ Cs\left(\vec{r}^{\,d}_m\right) \end{bmatrix}. \tag{7}$$

Matrix Z represents the coefficient matrix, which maps $u^{\text{sca}}(\vec{p})$ to $\text{Cs}(\vec{q})$, and $\mathbf{Z}(\vec{r}_p, \vec{r}_q) = k^2 G(\vec{r}_p, \vec{r}_q)\Delta V$, where ΔV represents the two-dimensional area unit.

Therefore, (2) can be written in matrix form as follows:

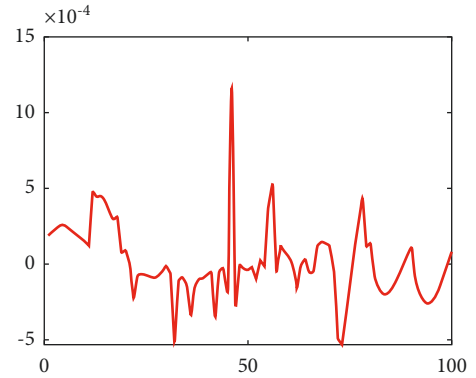

FIGURE 4: The error curve for inversion result of the *"U-shaped"* groove.

$$\begin{bmatrix} u^{\text{tot}}\left(\vec{r}^{\,d}_1\right) \\ \vdots \\ u^{\text{tot}}\left(\vec{r}^{\,d}_m\right) \end{bmatrix} = \begin{bmatrix} u^{\text{inc}}\left(\vec{r}^{\,d}_1\right) \\ \vdots \\ u^{\text{inc}}\left(\vec{r}^{\,d}_m\right) \end{bmatrix} + \begin{bmatrix} \mathbf{Z}\left(\vec{r}^{\,d}_1, \vec{r}^{\,d}_1\right) & \cdots & \mathbf{Z}\left(\vec{r}^{\,d}_1, \vec{r}^{\,d}_m\right) \\ \vdots & \ddots & \vdots \\ \mathbf{Z}\left(\vec{r}^{\,d}_m, \vec{r}^{\,d}_1\right) & \cdots & \mathbf{Z}\left(\vec{r}^{\,d}_m, \vec{r}^{\,d}_m\right) \end{bmatrix} \begin{bmatrix} Cs\left(\vec{r}^{\,d}_1\right) \\ \vdots \\ Cs\left(\vec{r}^{\,d}_m\right) \end{bmatrix}. \tag{8}$$

Since the scattered field data is known, (7) can be used to calculate the contrast source $Cs(\vec{r}^{\,d})$ according to the known scattered field data $u^{\text{sca}}(\vec{r}^{\,s})$. Then, since the incident field u^{inc} is known, the total field of the target area $u^{\text{tot}}(\vec{r}^{\,d})$ can be obtained using (8). Finally, according to (5), the parameter distribution of the target area can be obtained through known quantities $Cs(\vec{r}^{\,d})$ and $u^{\text{tot}}(\vec{r}^{\,d})$, after which the permittivity distribution of the target area can be resolved.

4. Numerical Simulation

In order to assess the performance of the proposed algorithm, this section introduces several examples of scatterers

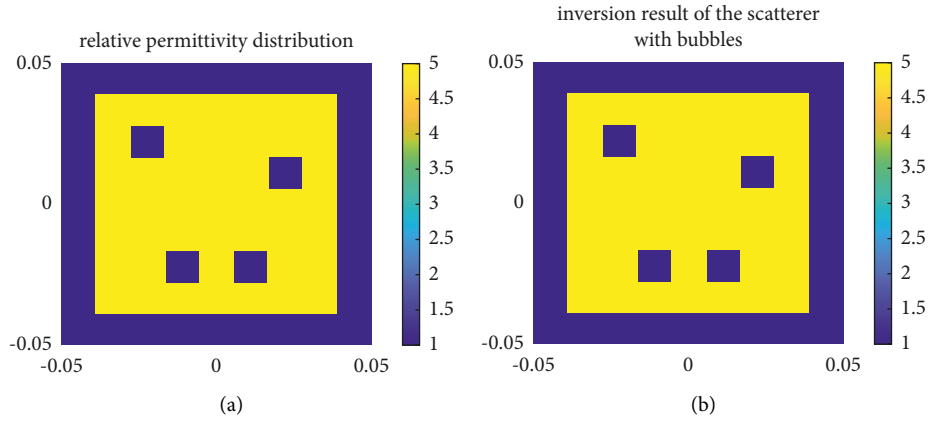

Figure 5: Comparison results of relative permittivity distribution of the scatterer with bubbles.

with different relative permittivity distributions. The incident frequency is 2.4 GHz, which is commonly applied in the ISM (Industrial Scientific Medical) frequency band. The imaging domain size is 0.1 m × 0.1 m. Three receiving circles are utilized, and 90 measuring points are distributed evenly on each circle. The excitation source is 0.25 m away from the center of the imaging domain. The measurement circles are 0.05 m, 0.10 m, and 0.15 m, respectively, from the imaging center.

4.1. "U-Shaped" Groove. This example employs a "U-shaped" groove as the scatterer. The side length of the "U-shaped" groove is 0.07 m, and the relative permittivity is set to 5. The original relative permittivity distribution and inversion result of the matrix algorithm are shown in Figure 3.

In order to compare the numerical values conveniently, the error curve which is obtained by the modulus of difference between the preset relative permittivity and the inversion result is shown in Figure 4. The abscissa represents the number of grids.

It can be seen from the two-dimensional inversion result and error curve that the matrix algorithm can solve the "U-shaped" groove imaging problem with a small error, which is distributed between $15^{*}10^{-4}$ and $-5^{*}10^{-4}$. The field coupling phenomenon between the inner groove of the "U-shaped groove" did not affect the imaging results.

4.2. Scatterer with Bubbles. A scatterer with several bubbles is employed in this example. Four bubbles are randomly located in an otherwise uniform scatterer, with each bubble measuring 0.01 m × 0.01 m. The size of the scatterer is 0.07 m × 0.07 m. The relative permittivity of the scatterer is 5. The original relative permittivity distribution and inversion result of the matrix algorithm are shown in Figure 5.

The error curve is shown in Figure 6.

It can be seen from the two-dimensional inversion result and error curve that the matrix algorithm can solve the scatterer with bubbles imaging problem with a small error, which is distributed between $2^{*}10^{-3}$ and $-2^{*}10^{-3}$. The position and number of bubbles are well reconstructed.

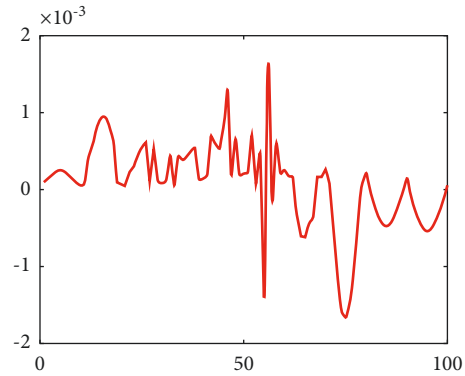

Figure 6: The error curve for the inversion result of the scatterer with bubbles.

4.3. Scatterer with Random Relative Permittivity. In this instance, a scatterer with a nonuniform distribution of relative permittivity is employed. The relative permittivity is generated using a random matrix with element values between 4 and 6. The relative permittivity value in each grid generated by the random matrix is relatively independent, which can effectively verify the performance of the proposed matrix algorithm in solving random problems. The original relative permittivity distribution and inversion result of the matrix algorithm are shown in Figure 7.

The one-dimensional error curve is shown in the following Figure 8.

It can be seen from the two-dimensional inversion result and error curve that the matrix algorithm can solve the scatterer with a random relative permittivity imaging problem with a small error, which is distributed between $2^{*}10^{-3}$ and $-2^{*}10^{-3}$.

4.4. Scatterer with Complex Permittivity. The relative permittivity in the previous three examples only have a real part, so in this instance, a complex permittivity is applied to assess the performance of the proposed algorithm. The scatterer has an "E-shaped" configuration, and the complex permittivity is set to $5 + 2i$. The original distribution of the real and imaginary parts of the relative permittivity is shown in Figure 9.

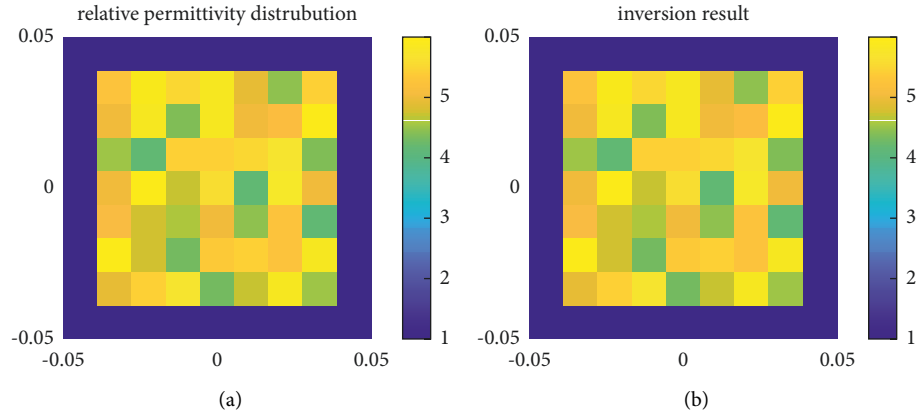

Figure 7: Comparison results of the relative permittivity distribution of the scatterer with random relative permittivity.

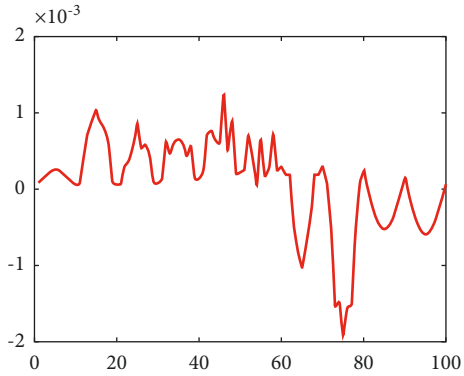

Figure 8: The error curve for the scatterer with random relative permittivity.

The inversion results obtained by the proposed algorithm are shown in Figure 10.

In order to accurately measure the performance of the matrix algorithm on the inversion of the complex permittivity, the parameter "correlation coefficient" is calculated. A correlation coefficient of 1 between the two sets of data implies that two sets have a strict linear relationship. Meanwhile, using the correlation coefficient for performance measurement does not need to compare the real and imaginary parts of the relative permittivity separately. After calculation, the correlation coefficient matrix between the original relative permittivity and the result of the matrix algorithm are as follows:

$$\begin{bmatrix} 1.0000 + 0.0000i & 1.0000 - 0.0002i \\ 1.0000 + 0.0002i & 1.0000 + 0.0000i \end{bmatrix}. \quad (10)$$

According to the correlation coefficient results, the two sets of permittivity results have a strict linear relationship. The error curve graphs are shown in Figure 11.

It can be seen from the two-dimensional inversion result and error curve that the matrix algorithm can solve the scatterer with a complex permittivity imaging problem with a small error. The error of the real part is distributed between $2 * 10^{-3}$ and $-2 * 10^{-3}$. The error of the imaginary part is distributed between 0 and $3 * 10^{-3}$.

4.5. Scatterer in Non-Free Space. Since the microwave imaging technology is widely utilized in medical imaging and earth exploration, the background space where the scatterer to be measured is located is not free in many cases, such as organic media and soil. Therefore, it is necessary to verify the performance of the proposed matrix algorithm on the scatterer in non-free space.

This example sets the relative permittivity of the background to $2 + 0.8i$, and the scatterer has two different relative permittivity, $1.5 + 0.3i$ and 10, respectively. The length of the outer side is 0.07 m, and the length of the inner side is 0.03 m. The relative permittivity distribution in the imaging domain is shown in Figure 12.

The inversion results obtained by the proposed algorithm are shown as follows in Figure 13.

The error curve graphs are shown in Figure 14 below.

It can be seen from the two-dimensional inversion result and error curve that the matrix algorithm can solve the imaging problem of the scatterer in non-free space with a small error. The error of the real part is distributed between $-4 * 10^{-3}$ and $2 * 10^{-3}$. The error of the imaginary part is distributed between $-2 * 10^{-3}$ and $10 * 10^{-3}$.

4.6. "U-Shaped" Groove under Different Measurement Points. In the above verification examples, the number of measurement points is fixed. This example verifies the performance of the proposed matrix algorithm by changing the number of measurement points. The scatterer and related preset parameter settings are consistent with the calculation example *A*, using the "U-shaped" groove with uniform relative permittivity distribution. The number of measurement circles is set to 3, and the number of measurement points evenly distributed on each measurement circle is set to 90, 60, 45, 40, and 30 in turn. The imaging results are shown in Figure 15.

It can be seen from the imaging results that with the decrease of the number of measurement points, the imaging quality shows a downward trend, the imaging results cannot well reflect the shape characteristics of the scatterer, and the imaging results inside the groove also show a downward trend.

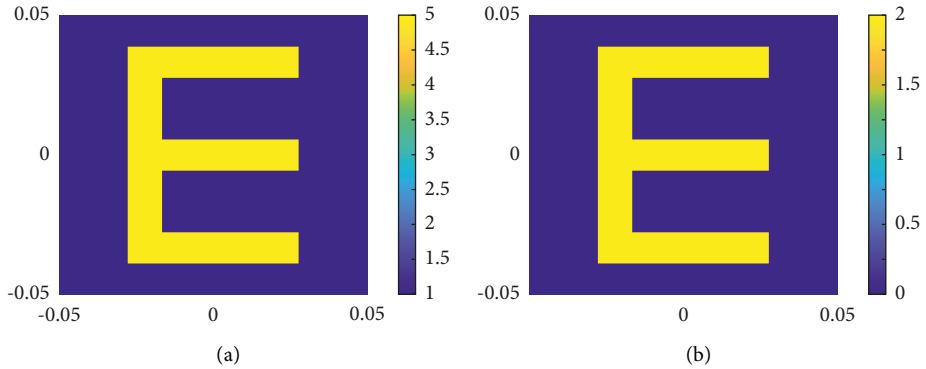

Figure 9: Original relative permittivity distribution. (a) Real part. (b) Imaginary part.

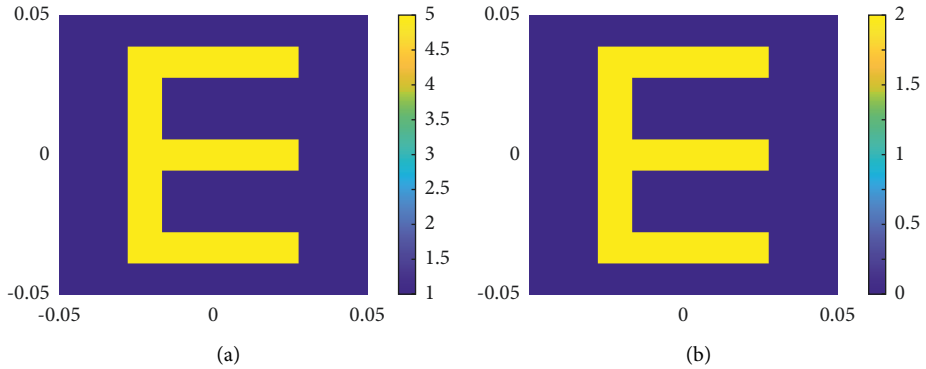

Figure 10: Inversion results of relative permittivity distribution. (a) Real part. (b) Imaginary part.

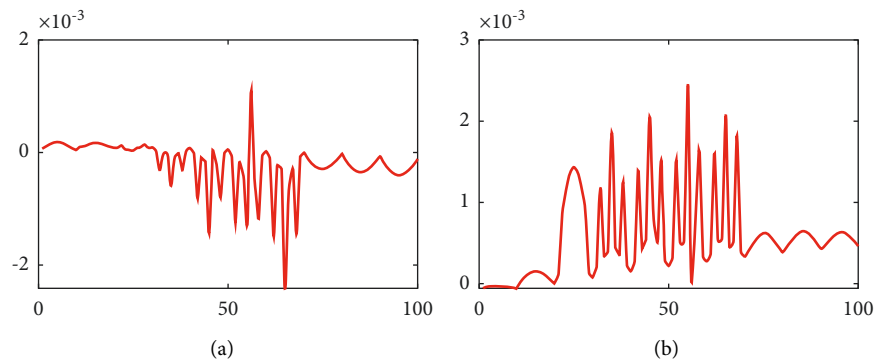

Figure 11: The error curves for the scatterer with complex permittivity. (a) Real part. (b) Imaginary part.

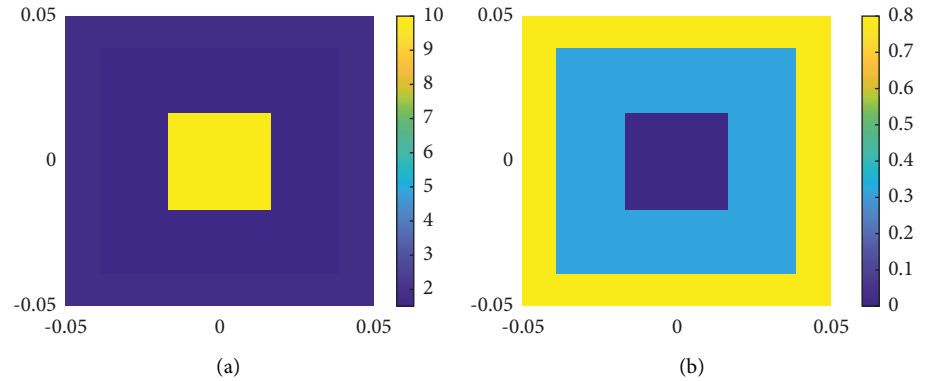

Figure 12: Relative permittivity distribution of the scatterer in non-free space. (a) Real part. (b) Imaginary part.

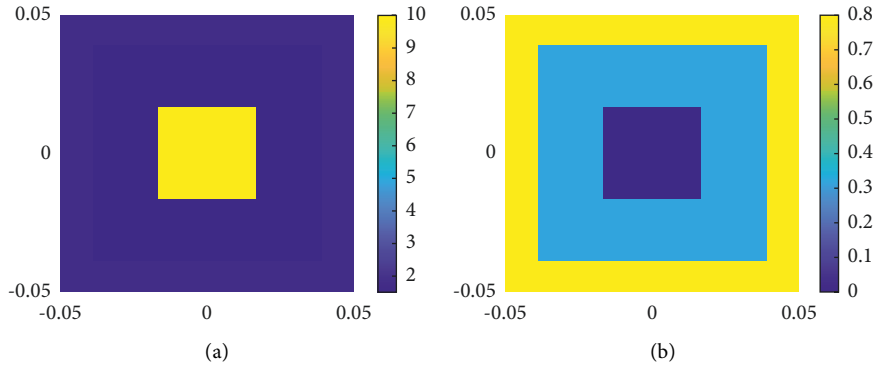

Figure 13: Inversion results of relative permittivity distribution of the scatterer in non-free space. (a) Real part. (b) Imaginary part.

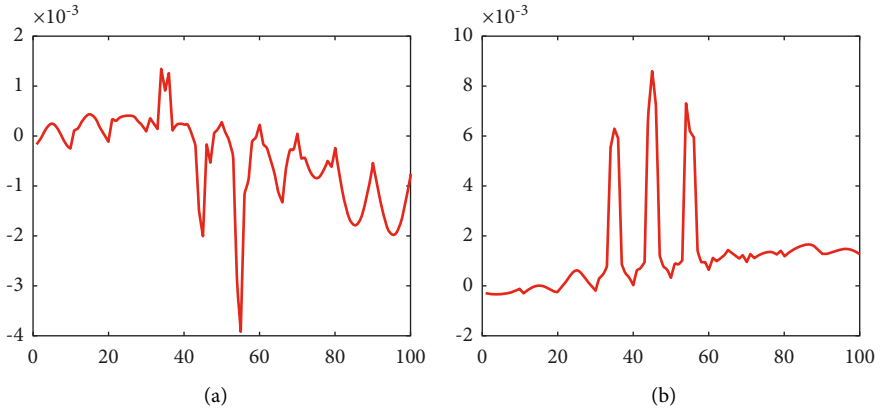

Figure 14: The error curves for the scatterer in non-free space. (a) Real part. (b) Imaginary part.

The errors of the imaging results are analyzed by using four parameters: the maximum error value, the minimum error value, the mean value, and the variance. The statistical data are shown in the following Table 1.

It can be seen from error statistics parameters that with the decrease of the number of measurement points, the maximum value of the reconstruction error gradually increases and the minimum value gradually decreases. Therefore, the mean and variance are changed at the same time, and the parameter performance shows a downward trend. From the solution analysis of the matrix problem, relative to the fixed number of unknown relative permittivity, with the reduction of the number of measurement points, the original matrix equation system becomes an underdetermined equation system, and the number of equations is less than the number of unknowns, resulting in nonunique solutions. Therefore, choosing an appropriate number of measurement points is helpful for the solution of the matrix algorithm.

4.7. "U-Shaped" Groove with Noise. It is necessary to test the robustness of the performance for the proposed algorithm. Therefore, in this example, noise with a fixed signal-to-noise ratio is added to the scattered field data, and the U-shaped groove is applied as the scatterer to verify the performance of the matrix algorithm. Scatterer parameters are the same as those of example A, and signal-to-noise ratios are set to 200, 150, 100, 80, 60, 40, and 20 in turn. The imaging results are shown in Figure 16.

It can be seen from the imaging results under different signal-to-noise ratios that with the decrease of the signal-to-noise ratio, the imaging quality shows an obvious.

4.7.1. Downward Trend. The shape and electromagnetic parameters of the scatterer cannot be well inverted. Therefore, it can be concluded that the proposed matrix algorithm has limitations for the inversion problem of scattered field data with noise.

From the derivation of the matrix algorithm, the proposed matrix algorithm has strict mathematical derivation and every parameter processes the physical meaning. However, in the process of matrix derivation, no processing method of noise removal is adopted. Therefore, although the matrix algorithm can obtain a high inversion accuracy, a little fluctuation may cause deviation of the solution result for matrix operation. Therefore, the proposed matrix algorithm does not have a strong robustness to noisy data.

4.8. Comparison with Another Algorithm. A hybrid algorithm based on the modified sine-cosine algorithm and the

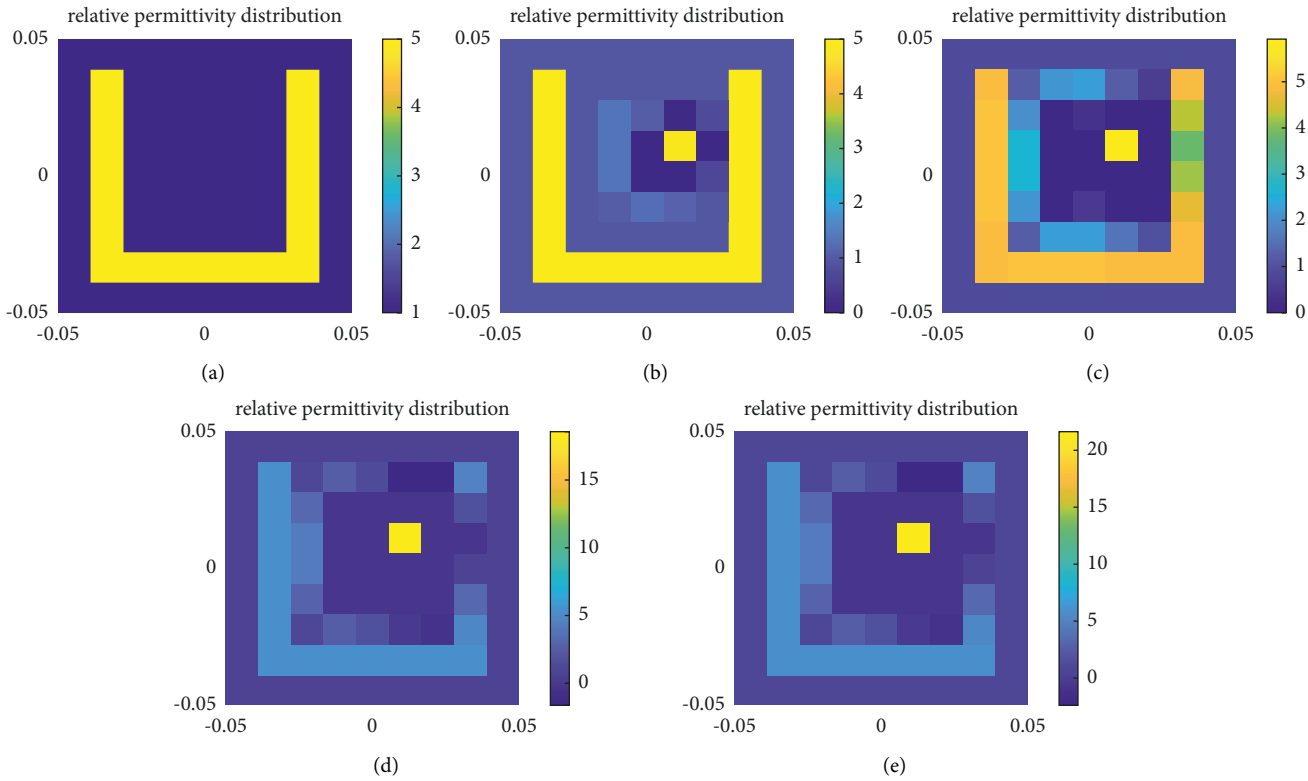

Figure 15: Imaging results with different number of measurement points. (a) The number is 90. (b) The number is 60. (c) The number is 45. (d) The number is 40. (e) The number is 30.

Table 1: Error parameters of imaging results under different number of measurement points.

Number of measuring points on each circumference	Number of measuring circumference	Maximum value	Minimum value	Mean	Variance
90	3	0.0012	−0.0005	$1.4867^{*}10^{--5}$	$5.7594^{*}10^{--8}$
60	3	1.0000	−4.1430	−0.0071	0.2186
45	3	1.1016	−8.9728	−0.0780	1.1419
40	3	5	−27.6275	−0.26195	8.98421
30	3	5	−33.7131	−0.35942	13.3044

least square method for solving optimization problems and microwave imaging problem was proposed in [11]. Since this hybrid algorithm adopted the parallel operation of two algorithms and the output result with the smallest error, it had a high precision. A ring scatterer for performance verification is applied in this example. Because the ring scatterer has an obvious field coupling phenomenon in the ring, it is suitable for performance verification of the imaging algorithm. The relative permittivity of the scatterer is set to $5 + 2i$, the outer side length is 0.07 m. The relative permittivity distribution of the real part and the imaginary part is shown in Figure 17.

The inversion results of relative permittivity obtained by the proposed matrix algorithm are shown in Figure 18.

The inversion results of relative permittivity obtained by the hybrid algorithm in [11] are shown in Figure 19.

The error curves of relative permittivity obtained by the two algorithms are shown in Figure 20.

It can be seen from the imaging results that both algorithms can perform a good inversion of the problem in this example, and the values of the real and imaginary parts are well reconstructed. It can be seen from the error curve that the error obtained by the hybrid algorithm proposed in [11] is much smaller than that of the proposed matrix algorithm. Then, from the operation time to consider, for the imaging problem in the example, the time required by the matrix algorithm is 0.3817s, and the time required by the hybrid algorithm in [11] is 83.1062s. Since iterative operation was required in the parallel algorithm in [11], the solution efficiency is lower than the proposed matrix algorithm, which requires no iterative operation. From a physical point of view, the matrix algorithm effectively avoids the black box solution and has a strict physical meaning. The hybrid algorithm in [11] was based on a stochastic optimization algorithm, and the physical meaning of parameters is weaker than the proposed matrix algorithm.

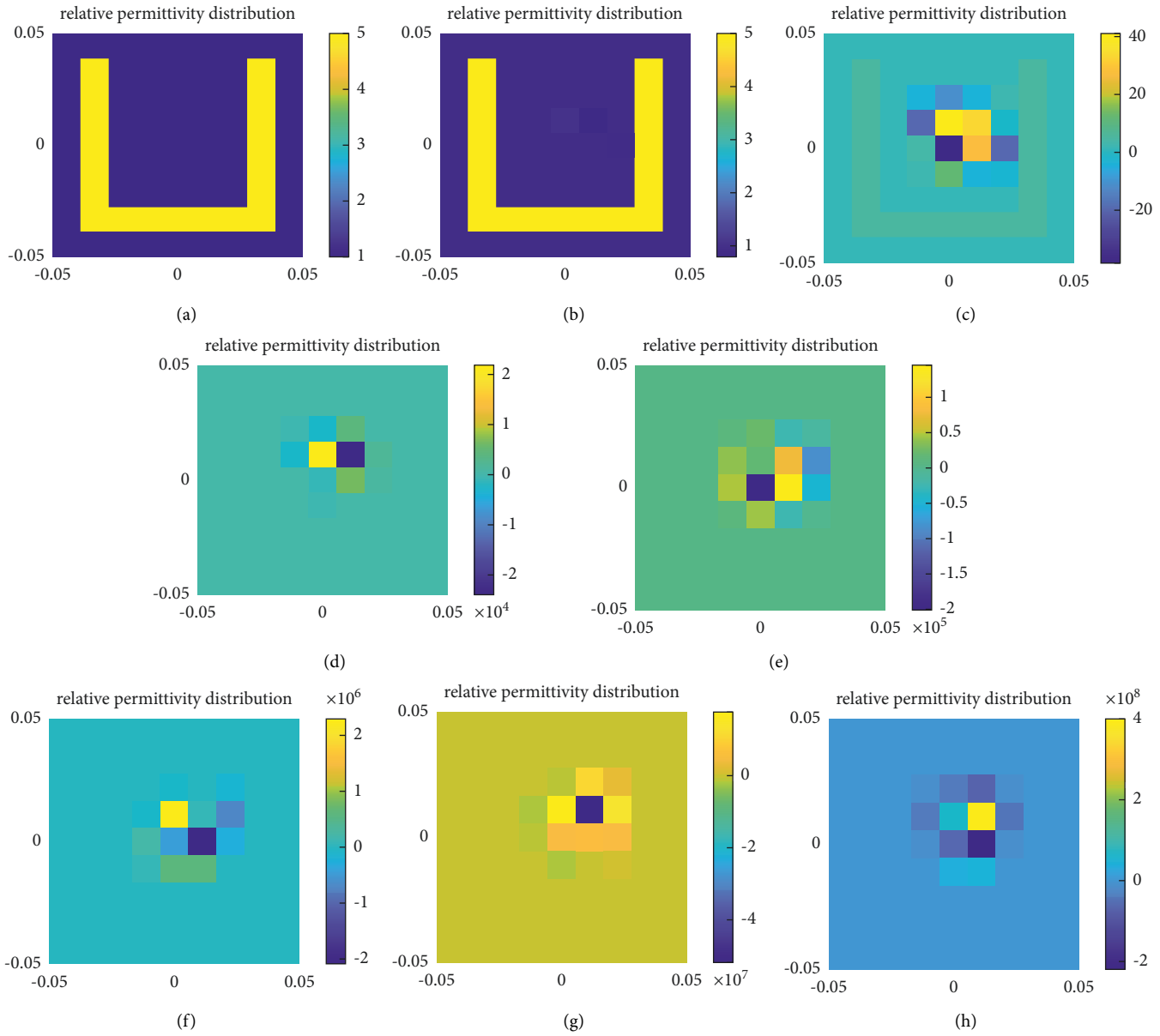

Figure 16: Imaging results with different signal-to-noise ratio. (a) No noise. (b) Snr = 200. (c) Snr = 150. (d) Snr = 100. (e) Snr = 80. (f) Snr = 60. (g) Snr = 40. (h) Snr = 20.

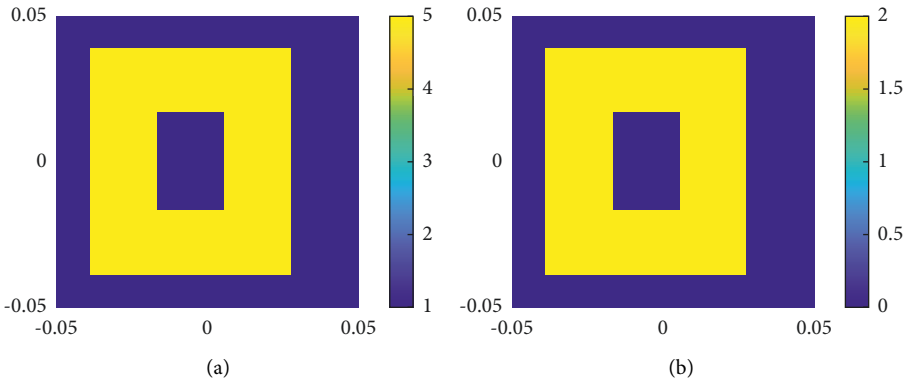

Figure 17: Relative permittivity distribution of ring scatterers. (a) Real part. (b) Imaginary part.

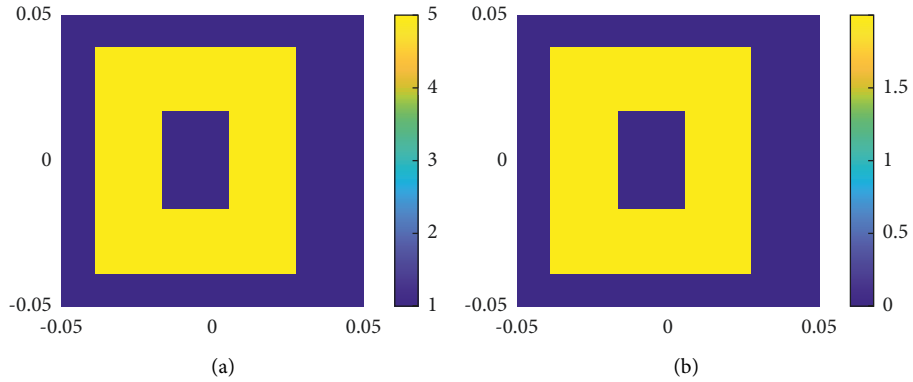

Figure 18: Inversion results obtained by proposed algorithm. (a) Real part. (b) Imaginary part.

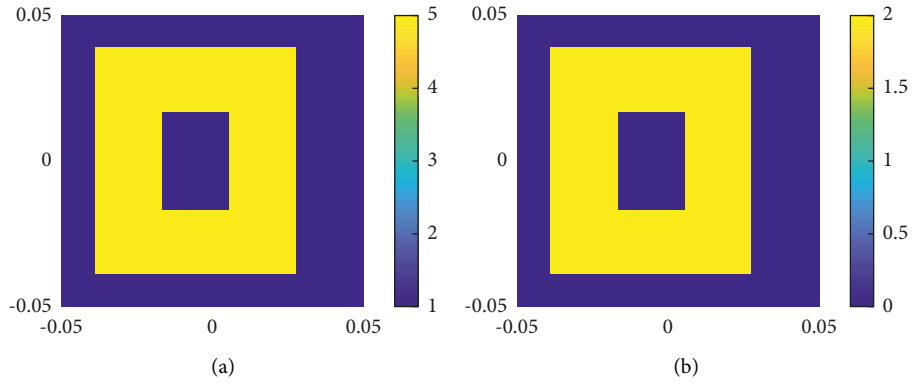

Figure 19: Inversion results obtained by hybrid algorithm in [11]. (a) Real part. (b) Imaginary part.

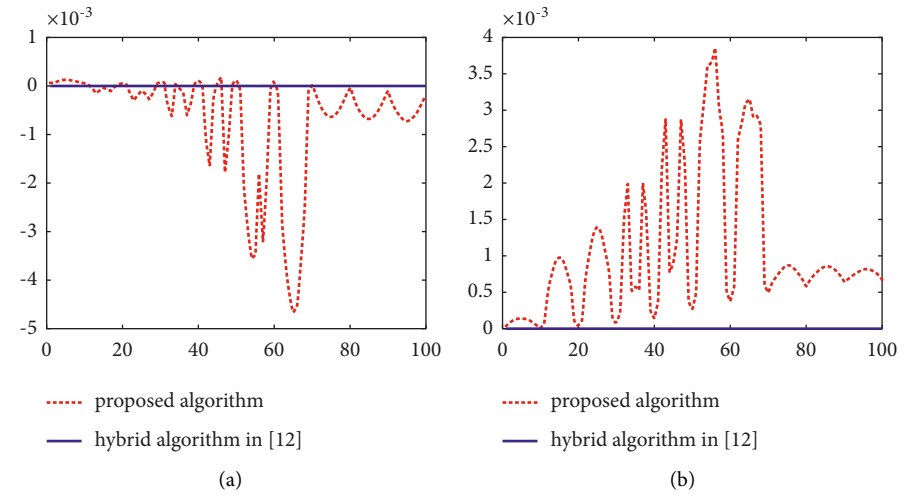

Figure 20: The error curves of relative permittivity obtained by the two algorithms. (a) Real part. (b) Imaginary part.

In summary, the proposed microwave imaging matrix algorithm can effectively solve the complex imaging problems listed above. The shape, position, and relative permittivity of scatterers are inversed well. The order of the error obtained is relatively low. Because the proposed matrix algorithm transforms the ill-conditioned imaging problem into the calculation of the matrix step-by-step, it needs no iterative calculations. For the current computer, matrix operation without iteration can obtain a lower time cost and hardware cost. In addition, the microwave imaging matrix algorithm is based on Lippmann–Schwinger equation and a contrast source, which has the strict physical directivity. Therefore, it can be utilized to a wide range of imaging problems. However, the proposed matrix algorithm does not achieve a strong robustness when solving a microwave imaging problem with noise.

5. Conclusion

This paper introduces a microwave imaging matrix algorithm based on a contrast source. First, in order to ensure the constancy of the contrast source, an improved inversion model is proposed, employing a fixed excitation source and several measuring points evenly distributed on multiple circles. Second, a matrix algorithm is proposed based on the contrast source and an improved inversion model. The most significant innovation is that iterative operation is not required in the proposed algorithm, which is more suitable for diverse imaging problems. Meanwhile, the algorithm proposed has strict mathematical and physical derivation, avoiding traditional "black box" methods. Various simulation examples are then explored, where it is shown that the proposed algorithm can achieve high imaging accuracy. Meanwhile, the effect of the number of measurement points on the performance of the proposed algorithm is studied. In addition, the robustness of the matrix algorithm has been verified and analyzed.

Our future work will apply this proposed approach to high-dimensional and broader inverse scattering problems and study corresponding improvement methods in view of the limitations of existing algorithms in dealing with noisy data.

Data Availability

The data used to support the findings of this study are available from the corresponding author upon request.

Conflicts of Interest

The authors declare that they have no conflicts of interest.

Acknowledgments

The authors gratefully acknowledge the support of the Beijing Institute of Environmental Properties, who provided grant no. 621802Y030204.

References

[1] R. Chandra, H. Zhou, I. Balasingham, and R. M. Narayanan, "On the opportunities and challenges in microwave medical sensing and imaging," *IEEE Transactions on Biomedical Engineering*, vol. 62, no. 7, pp. 1667–1682, 2015.

[2] M. F. Imani, J. N. Gollub, O. Yurduseven et al., "Review of metasurface antennas for computational microwave imaging," *IEEE Transactions on Antennas and Propagation*, vol. 68, no. 3, pp. 1860–1875, 2020.

[3] M. Pastorino, "Stochastic optimization methods applied to microwave imaging: a review," *IEEE Transactions on Antennas and Propagation*, vol. 55, no. 3, pp. 538–548, 2007.

[4] P. M. v. d. Berg and R. E. Kleinman, "A contrast source inversion method," *Inverse Problems*, vol. 13, no. 6, pp. 1607–1620, 1997.

[5] S. Sun, B.-J. Kooij, and A. G. Yarovoy, "Inversion of multi-frequency data with the cross-correlated contrast source inversion method," *Radio Science*, vol. 53, no. 6, pp. 710–723, 2018.

[6] K. Kuiwen Xu, Y. Yu Zhong, R. Rencheng Song, X. Lixin Ran, and L. Ran, "Multiplicative-regularized FFT twofold subspace-based optimization method for inverse scattering problems," *IEEE Transactions on Geoscience and Remote Sensing*, vol. 53, no. 2, pp. 841–850, 2015.

[7] Y. Zhang, Q. Zhao, Z. Zhao, and Z. Nie, "A hierarchical subspace-based optimization method for reconstruction of 2-D uniaxial anisotropic scatterers using multi-frequency data," *IEEE Transactions on Magnetics*, vol. 57, no. 7, pp. 1–4, 2021.

[8] M. T. Bevacqua and R. Scapaticci, "A compressive sensing approach for 3D breast cancer microwave imaging with magnetic nanoparticles as contrast agent," *IEEE Transactions on Medical Imaging*, vol. 35, no. 2, pp. 665–673, 2016.

[9] Z. Wei and X. Chen, "Physics-inspired convolutional neural network for solving full-wave inverse scattering problems," *IEEE Transactions on Antennas and Propagation*, vol. 67, no. 9, pp. 6138–6148, 2019.

[10] T. Isernia, V. Pascazio, and R. Pierri, "A nonlinear estimation method in tomographic imaging," *IEEE Transactions on Geoscience and Remote Sensing*, vol. 35, no. 4, pp. 910–923, 1997.

[11] M. Wang and G. Lu, "A hybrid algorithm based on a modified sine cosine algorithm and least square and its application to microwave imaging," *International Journal of Antennas and Propagation*, vol. 2021, Article ID 6678876, 12 pages, 2021.

[12] Y. Su and G. Lu, "An improved inversion model for two-dimensional microwave imaging," in *Proceedings of the 2019 Cross Strait Quad-Regional Radio Science and Wireless Technology Conference (CSQRWC)*, pp. 1–3, Taiyuan, China, July 2019.